

E or IRAS2), more pronounced than toward VLA1+VLA2, which can be reproduced only by assuming a colder, optically thick emission for the central source. Hence, the observed behavior rules out the possibility of a dust jet origin of moderate column density (optically thin) for the emission in the innermost region. Nevertheless, the dusty jet is detected as an extended component in our maps (Fig. 1) and makes a contribution to the continuum emission in the 5- to 17- $\mu\text{m}$  spectra observed with ISOCAM.

The large amount of ices found around these sources shows that molecular depletion onto dust grains is a major process in the cold dense regions where low-mass stars form. The profile of the ices' absorption varies from source to source (see Fig. 2), but in all of them the three mid-IR windows are present. In addition to the ices of  $\text{H}_2\text{O}$ ,  $\text{CH}_3\text{OH}$ , and  $\text{CO}_2$ , the observed spectra toward the low-mass protostars shown in Fig. 2 indicate the presence of  $\text{CH}_4$  and of another ice absorber at 7.35  $\mu\text{m}$ . The amount of each component depends on the chemical evolution of the protostellar condensation. In addition, the dust in the protoplanetary disk could be heated by the radiation from the central object or from the shocks associated to the accretion processes, leading to evaporation of volatile species. The dust grains, which initially contain amorphous silicates, could be submitted to a transition phase in the evolution of the protostar region toward a stellar object and its protoplanetary disk. The temperatures we derive for the central class 0 objects are high enough to make such phase transitions possible in the innermost regions of the protoplanetary disks. In this context, we note that the spectrum toward the CS star (Fig. 1C) exhibits a broad band in emission that suggests the presence of crystalline silicates (28).

The good agreement between the observed luminosity at millimeter wavelengths and the predicted value for the emitting source in the few central astronomical units of VLA1+VLA2 closely relates the origin of the emission in the mid-IR and that observed at longer wavelengths from the extended cold dust. We therefore suggest that the emission detected through the three mid-IR windows traces the few inner astronomical units of the warm protoplanetary envelope (disk) around the accreting protostar, which is deeply embedded in a much larger cold core. We cannot exclude the possibility that the IR emission observed toward the sources comes from a more evolved companion; however, among the sources shown here, signs of multiple components in the protostellar core have been reported only toward L1448-C.

The present classification of protostars does not consider the range of concentrations of ices and silicates in the protostellar envelope, nor does it consider the nature of the hot central object evident in the ISO data. This classifica-

tion scheme is more representative of the properties of the outer cold dust envelope than of the physical properties and processes in the innermost regions, where the star and its protoplanetary system are being formed.

References and Notes

1. P. André, D. Ward-Thompson, M. Barsony, *Astrophys. J.* **406**, 122 (1993).
2. C. J. Lada, in *The Physics of Star Formation and Early Stellar Evolution*, C. J. Lada and N. D. Kylafis, Eds. (Kluwer Academic, Dordrecht, Netherlands, 1991), pp. 329–363.
3. F. C. Adams, C. J. Lada, F. Shu, *Astrophys. J.* **312**, 788 (1987).
4. J. Cernicharo and B. Reipurth, *Astrophys. J.* **460**, L57 (1996).
5. B. Reipurth and J. Cernicharo, *Rev. Mex. Astron. Astrophys. (Ser. Conf.)* **1**, 43 (1995).
6. A. Moro-Martín, J. Cernicharo, A. Noriega-Crespo, J. Martín-Pintado, *Astrophys. J.* **520**, L111 (1999).
7. R. Bachiller, *Annu. Rev. Astron. Astrophys.* **34**, 111 (1996).
8. C. R. O'Dell and V. W. Beckwith, *Science* **276**, 1355 (1997).
9. G. Pelletier and R. E. Pudritz, *Astrophys. J.* **394**, 117 (1992).
10. F. Shu *et al.*, *Astrophys. J.* **429**, 797 (1994).
11. C. J. Cesarsky *et al.*, *Astron. Astrophys.* **315**, L32 (1996).
12. M. F. Kessler *et al.*, *Astron. Astrophys.* **315**, L27 (1996).

13. J. J. Hester, K. R. Stapefeldt, P. A. Scowen, *Astron. J.* **116**, 372 (1998).
14. G. H. Herbig, *Astrophys. J.* **113**, 697 (1951).
15. G. Haro, *Astrophys. J.* **115**, 572 (1952).
16. S. H. Pravdo *et al.*, *Astrophys. J.* **293**, L35 (1985).
17. R. Chini *et al.*, *Astron. Astrophys.* **325**, 542 (1997).
18. P. André, D. Ward-Thompson, M. Barsony, in *Protostars and Planets IV*, V. Mannings, A. P. Boss, S. S. Russell, Eds. (Univ. of Arizona Press, Tucson, AZ, 2000).
19. B. Reipurth, S. Heathcote, N. Roth, A. Noriega-Crespo, A. C. Raga, *Astrophys. J.* **408**, L49 (1993).
20. L. F. Rodríguez *et al.*, in preparation.
21. L. d'Hendecourt *et al.*, *Astron. Astrophys.* **315**, L365 (1996).
22. W. A. Schutte *et al.*, *Astron. Astrophys.* **315**, L333 (1996).
23. D. C. B. Whittet *et al.*, *Astron. Astrophys.* **315**, L357 (1996).
24. E. Dartois, thesis, Université Paris VI (1999).
25. P. A. Gerakines, W. A. Schutte, P. Ehrenfreund, *Astron. Astrophys.* **312**, 289 (1996).
26. D. M. Hudgins, S. A. Sandford, L. J. Allamandola, A. G. G. M. Tielens, *Astrophys. J. Suppl. Ser.* **86**, 713 (1993).
27. K. Demyk, personal communication.
28. B. Lefloch, J. Eisloffel, B. Lazareff, *Astron. Astrophys.* **313**, L17 (1996).
29. We thank Spanish Dirección General de Enseñanza Superior and Plan Nacional de Investigación Espacial for support under grants PB96-0883 and PB98-1351E.

22 November 1999; accepted 21 March 2000

## Control of Energy Transfer in Oriented Conjugated Polymer–Mesoporous Silica Composites

Thuc-Quyen Nguyen, Junjun Wu, Vinh Doan, Benjamin J. Schwartz,\* Sarah H. Tolbert\*

Nanoscale architecture was used to control energy transfer in semiconducting polymers embedded in the channels of oriented, hexagonal mesoporous silica. Polarized femtosecond spectroscopies show that excitations migrate unidirectionally from aggregated, randomly oriented polymer segments outside the pores to isolated, aligned polymer chains within the pores. Energy migration along the conjugated polymer backbone occurred more slowly than Förster energy transfer between polymer chains. The different intrachain and interchain energy transfer time scales explain the behavior of conjugated polymers in a range of solution environments. The results provide insights for optimizing nanostructured materials for use in optoelectronic devices.

One of the outstanding challenges in the design of nanostructured materials is the fabrication of systems that allow the flow of energy to be controlled and directed to regions useful for a desired purpose. In the photosynthetic reaction center, for example, light en-

ergy harvested at multiple sites spontaneously flows to the appropriate location in the complex so that electron transfer can take place (1). In attempts to mimic this type of behavior, scientists have linked chromophores with continually decreasing band gaps along polymer chains (2) or layered chromophores in thin film heterostructures (3, 4). Although good directional energy transfer can be achieved in these systems, energy is lost because large differences in the emission energy of each successive chromophore are needed.

Department of Chemistry and Biochemistry, University of California, Los Angeles, Los Angeles, CA 90095–1569, USA.

\*To whom correspondence should be addressed. E-mail: tolbert@chem.ucla.edu and schwartz@chem.ucla.edu

We show how control over energy flow can be achieved in an artificial system consisting of semiconducting polymer (5, 6) chromophores that have been aligned on the nanometer scale and encapsulated into the hexagonally arrayed channels of mesoporous silica glass (7, 8). The design of the system forces energy to flow along single polymer chains into the oriented, periodic component of the composite material. The driving force for this energy flow arises solely from changes in polymer conformation: the short conjugation-length polymer segments outside the silica framework have a higher energy than the long conjugation-length polymer segments encapsulated within the channels. As a result, energy migration in this composite system produces a spontaneous increase in luminescence polarization with minimal decrease in fluorescence energy. Thus, nanometer-scale positional control achieved through host-guest chemistry and the sensitive optical properties of semiconducting polymers can be combined to control energy flow. Moreover, the composites also allow us to separate the role of interchain versus intrachain energy transfer in conjugated polymers, providing valuable information for the optimization of polymer-based optoelectronic devices.

The chromophore we chose is the semiconducting polymer poly[2-methoxy-5-(2'-ethylhexyloxy)-1,4-phenylene vinylene] (MEH-PPV), whose chemical structure and photoluminescence (PL) spectrum are shown in Fig. 1. Bends or twists of the polymer chain result in breaks in the  $\pi$  conjugation. For conjugated polymers in solution or films, these kinks produce chromophores with a wide range of conjugation lengths. Because the excitation energy is a strong function of conjugation length, the polymer displays an inhomogeneous distribution of absorption energies. Time-resolved studies on conjugated polymers have established that energy can transfer rapidly between polymer segments with different conjugation lengths (9–13) or between polymer segments and other chromophores (14–17) via Förster transfer (18, 19) (dipole-dipole coupling). The Förster transfer time, just a few picoseconds (9, 10, 13, 14, 18), is much faster than the emission lifetime, so emission is usually observed only from the longest, lowest energy segments. For example, the PL emission from MEH-PPV in a solution of chlorobenzene (CB) is redshifted from that in tetrahydrofuran (THF) (Fig. 1A) because the polymer chains in CB are less tightly coiled and thus have a longer average conjugation length (20). Overall, the ability of excitations to explore a range of polymer environments rapidly and the strong dependence of excitation energy on conjugation length allow us to control energy migration in nanostructured materials containing these polymers.

We use mesoporous silica-polymer host-guest chemistry (21–24) to control the polymer chain configuration and the energy flow by

placing MEH-PPV into the oriented, hexagonally arrayed channels (22 Å diameter) of a mesoporous silica glass (25). The synthesis makes use of a nanoporous silica host that was aligned in a magnetic field with a silica-surfactant liquid-crystalline intermediate (26). After condensation and calcination of the silica host (27), the resulting mesoporous silica was surface-treated with organic groups. Polymer chains were incorporated from solution and the resulting composite is index-matched in a glycerol/propanol mixture to suppress scattering from the domain structure of the silica framework. Polarized steady-state luminescence (Fig. 1, B and C) shows that incorporation of MEH-PPV into the oriented porous silica host leads to alignment of the polymer chains (25). With excitation parallel to the aligned axis of the pores, a polarization ratio (parallel:perpendicular) of 4.5:1 is observed, compared with a value of  $\sim 1.4$ :1 for neat polymer films. A detailed modeling of the luminescence in which the distribution of pore angles from x-ray diffraction is used indicates that  $\geq 80\%$  of the polymers in the composite samples are aligned and are inside the pores (25). The remaining 20% of the chromophores are in a different environment; either partially hanging out of the pore or adsorbed onto the outside of one of the domains. Note that physically there is room for only one polymer chain per pore (25). Thus, the polymer chains inside these composites are not just isolated but are individually encapsulated

in a dielectric 2 to 3 nm thick, eliminating energy transport between chains.

The environment in which a polymer chain resides can be characterized by monitoring the dynamics of the polymer's excited-state absorption. Many studies have shown a rapid, nonexponential transient absorption decay in phenylene-vinylene polymer films, whereas slower, single exponential decays are observed from isolated chains in solution (28–30). Because the polymer chains inside the pores are uniaxially aligned but those outside are randomly oriented, we can use femtosecond polarized transient absorption spectroscopy to probe separately the different polymer environments inside and outside the pores. Exciting and probing with polarization parallel to the pore direction will preferentially measure the dynamics of polymer chains in the interior of the pores; the use of light that is polarized perpendicularly to the pore direction will favor absorption from the randomly oriented polymer segments outside the pores. The details of our ultrafast apparatus, which has an instrumental resolution of  $\sim 200$  fs, are described elsewhere (20, 30). Briefly, our samples were excited with a polarized ultrafast laser pulse centered at 490 nm, the peak of the MEH-PPV absorption spectrum. The excited state dynamics were monitored with a variably delayed polarized probe pulse centered near the excited-state absorption maximum of 800 nm. The crosses and circles in Fig. 2 show the 800-nm absorption decay of excited MEH-PPV

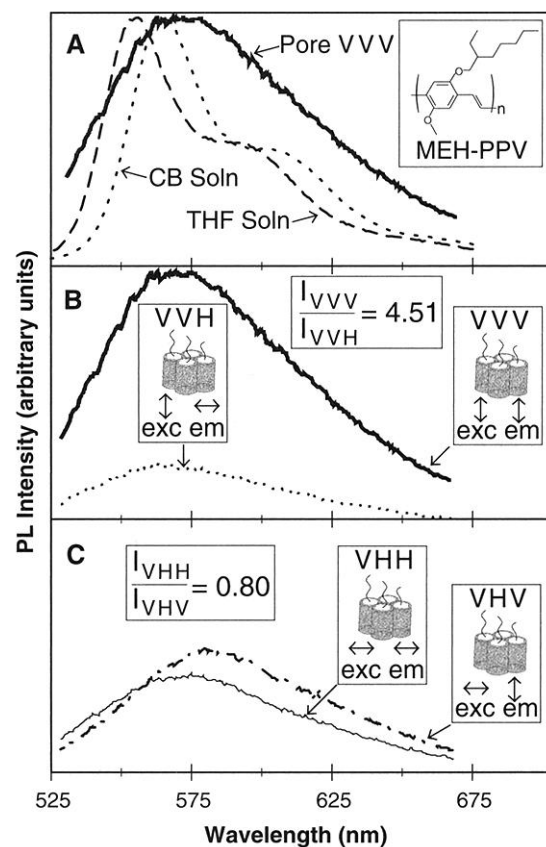


**Fig. 1.** (A) Steady-state PL spectra of MEH-PPV in different environments as follows: CB solution (dashed curve), THF solution (dotted curve), and the mesoporous silica composite with excitation and collection polarizations parallel to the pore direction (VVV, heavy solid curve). The three curves are scaled for ease of comparison. The inset shows the chemical structure of MEH-PPV. (B) PL of MEH-PPV in the nanostructured composite with excitation (exc) light polarized along the pore direction. The heavy solid curve [VVV, same as in (A)] shows emission (em) collected polarized along the pore direction. The dotted curve (VVH) is for emission collected polarized perpendicular to the pore direction. (C) PL of MEH-PPV in the nanostructured composite with excitation light polarized perpendicular to the pore direction. The dot-dashed curve (VHH) shows emission collected polarized along the pore direction, and the thin solid curve is for emission collected polarized perpendicular to the pores (VHV). The relative intensities of the four curves in (B) and (C) are as measured and have not been scaled.

in a CB solution and in a spin-cast film, respectively. In agreement with previous work (28, 31, 32), we found a long-lived, single exponential decay in solution and a more complex, rapid decay when the chains are in contact in the polymer film. With the channels on the composite sample oriented vertically (V) in the lab and vertically polarized (V) excitation, the solid curve in Fig. 2 depicts the vertically polarized (V) excited-state absorption dynamics (together, the three orientations are denoted as VVV) (33). The horizontally polarized absorption dynamics after horizontal excitation (VHH) are shown as the dashed curve. The VVV transient absorption decay is quite similar to that of the polymer in solution, whereas the VHH excited-state decay closely matches that of the polymer film. Clearly, the excited-state absorption transients show that the aligned polymer chains inside the pores are isolated in a solution-like environment, and that the randomly oriented chains outside the pores have a degree of interchain contact similar to that in the film.

Next, we used both steady-state and time-resolved luminescence to monitor energy transfer in our composites, thus probing the fate of the emissive excitons created on the polymer chains after energy transfer. A particularly striking result from steady-state measurements is that when exciting with light polarized perpendicular to the pore direction, more light is emitted polarized in the direction along the pores (Fig. 1C, dot-dashed curve, VHV) than along the direction of excitation (Fig. 1C, thin solid curve, VHH). Moreover, the light emitted polarized parallel to the pores is redshifted relative to the light emitted along the excitation direction. This result suggests that excitons on conjugated polymer segments outside the pores, which are preferentially excited by the light polarized against the pore direction, migrate to lower energy segments inside the pores where they emit light that is redshifted and polarized along the pore direction.

Insight into the dynamics of this directional energy migration into the pores can be obtained by time-resolved stimulated emission anisotropy. After femtosecond excitation at 490 nm, the polarized luminescence dynamics were measured via stimulated emission with a variably delayed probe pulse centered near the PL maximum of 590 nm. In the absence of energy migration, the emitted light would tend to have the same polarization as the excitation laser. However, when energy transfers to a new segment with a different physical orientation, memory of the initial excitation polarization is lost until eventually there is no difference in intensity for light emitted polarized either parallel ( $\parallel$ ) or perpendicular ( $\perp$ ) to that of the excitation laser. The quantity we report as a measure of the polarization memory is the time-dependent anisotropy,  $r(t)$  (34)

$$r(t) = \frac{\parallel(t) - \perp(t)}{\parallel(t) + 2\perp(t)} \quad (1)$$

The absolute magnitudes of the  $\parallel$  and  $\perp$  emission transients are somewhat difficult to measure because many of the optics in the experimental setup have polarization-dependent reflectivities. Thus, in the results presented below, we have integrated the measured  $\parallel$  and  $\perp$  polarization dynamics and scaled them to match the relative magnitudes of the polarized steady-state luminescence at the same wavelength.

Figure 3 shows the dynamic stimulated emission anisotropy from the composite sample when the excitation laser is polarized along the direction of the pores. The initial value of the anisotropy,  $r(0) = 0.53$ , is larger than 0.4, indicating the alignment of energy in the composite is greater than in isotropic samples, as expected. There is a small initial rapid loss of anisotropy in the first few picoseconds, which on the basis of previous energy transfer studies (9, 10, 13, 14, 18) we assign to interchain energy transfer between the  $\sim 20\%$  of the conjugated polymer segments in the film-like environment outside the pores. However, after the rapid decay, we see an increase in the anisotropy, which eventually tapers off at a value greater than  $r(0)$ ; the nanoscale architecture of the composite sample causes the energy to become spontaneously more aligned with time. The solid line in Fig. 3 is a fit to a 250-ps exponential rise (35). Although an anisotropy rise could be produced artifactually if the polymer chro-

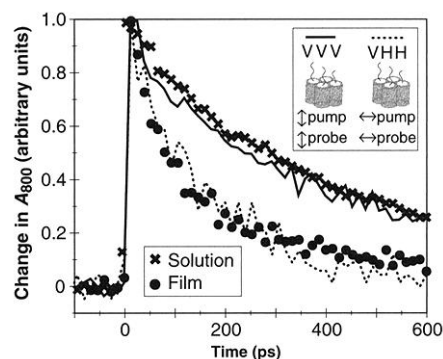


**Fig. 2.** Ultrafast transient absorption dynamics of MEH-PPV in different environments probed at 800 nm after excitation at 490 nm, normalized to the same intensity at time 0. The crosses and circles show the excited state absorption decay of MEH-PPV in a CB solution and in a spin-coated film, respectively. For MEH-PPV in the mesoporous silica composite, the solid curve is the absorption decay with the pump and probe pulse polarizations parallel to the pore direction (VVV, see inset), and the dotted curve shows the absorption dynamics with pump and probe polarizations perpendicular to the pore direction (VHH). All four curves were taken under identical excitation conditions; typical signal sizes were a change in optical density of a few percent.

mophores in the two environments had different emission lifetimes, the steady-state data shown in Fig. 1C and the intensity independence of the data shown in Fig. 3 eliminates this possibility. The only way to explain both the increase in the time-dependent anisotropy (Fig. 3) and a steady-state fluorescence polarization ratio less than 1 (Fig. 1C) is with migration of excitons from the coiled and nonaligned high-energy segments outside the pores to the straight and oriented low-energy segments encapsulated in the pores.

The data shown in Fig. 1C also allow us to quantify the magnitude of the energy migration observed in Fig. 3. Directional migration of excitons from the randomly oriented portion of the composite into the silica nanopores results in a 30% increase in the intensity of the cross-polarized luminescence relative to that in neat polymer films (25). Because the composite samples are designed to have room for only one chain per pore, the exciton migration that produces this 30% increase must take place along the polymer backbone. Thus, by forcing energy to flow along single polymer chains, the design of our nanostructured system takes energy deposited with random orientation outside the pores and directs it to the aligned chromophores within the pores. By analogy with the photosynthetic reaction center, the aligned polymer chains within the pores of our composite behave as guides for the energy harvested from the polymer segments outside the pores, the antenna chromophores. This type of directed energy transfer requires nanoscale complexity with two different environments and thus cannot take place in

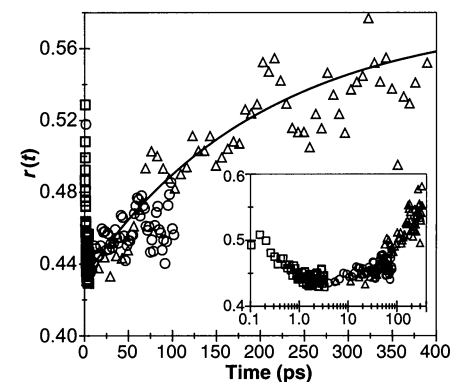


**Fig. 3.** Ultrafast stimulated emission anisotropy (Eq. 1) of MEH-PPV encapsulated in mesoporous silica glass with the excitation pulse polarization parallel to the pore direction. The solid curve in the figure is a 250-ps exponential rise. The excitation and probe wavelengths are 490 and 590 nm, respectively. The different symbols represent scans taken with different amounts of time between points:  $\square$ , 0.067 ps per point;  $\circ$ , 1.67 ps per point;  $\triangle$ , 6.67 ps per point. The inset shows the same data with a log scale for the time axis so that the early time data are more visible.

simpler systems consisting of conjugated polymers aligned by tensile drawing (36, 37).

The anisotropy data from the composite samples also suggests that although energy migration between polymer chains is fast, migration along a chain is unexpectedly slow. For this discussion, we define interchain energy migration as the through-space Förster transfer between two polymer segments that are in close proximity. Thus, Förster energy transfer between segments on two different polymer chains and transfer between two distant segments of the same chain are both labeled as interchain transfer. By contrast, we define intrachain energy migration as energy migration between two neighboring segments along the backbone of a single polymer chain. Note that the transition dipoles in these materials are oriented along the chain axis, so intrachain energy migration cannot occur via Förster transfer. Figure 4 shows the time-resolved stimulated emission anisotropy for MEH-PPV in three different solution environments: dilute and concentrated THF and dilute CB solutions. Like the composite samples, the anisotropy transients we measure in solution are characterized by a rapid initial decay that is complete within a few picoseconds. The rapid decay is then followed by a plateau, or, at high concentrations, a much slower decay occurs with a  $\sim 250$ -ps exponential time constant.

On the basis of our understanding of energy migration in polymer in the silica nanopores, we assign the rapid anisotropy decay to interchain energy transfer. However, this conclusion is contrary to previous interpretations of similar data, which assigned the rapid anisotropy loss to energy migration along the polymer backbone (38–40). This assignment to interchain transfer is based on the correlation of the magnitude of the initial anisotropy loss with the greater degree of aggregation of MEH-PPV in

CB relative to THF (20). Increased aggregation allows more Förster transfer between polymer chains in CB than in THF at the same concentration, which results in the larger initial loss of anisotropy in CB seen in Fig. 4. Förster transfer is likely further enhanced in CB solutions because  $\pi$  stacking also increases the probability of transition. The assignment of the fast anisotropy decay to interchain transfer between aggregated chains is also supported by the increase in magnitude of the fast decay in THF solutions when aggregation is promoted by increasing the polymer concentration (20). Figure 4 also shows that at high concentrations, however, a second slow anisotropy decay appears, which has the same time constant as the rise observed in Fig. 3.

We can explain the appearance of this slow anisotropy decay as well as all data presented in Figs. 3 and 4 as follows: Interchain transfer takes place in a few picoseconds between those conjugated polymer segments that are physically located within a Förster transfer radius. Once the energy has migrated sufficiently, there are no lower energy segments close enough for Förster transfer to occur, so interchain energy transfer ceases. Excitons can continue to migrate along the polymer backbone, but, as is evident from Fig. 3, they do so quite slowly, on a time scale of a few hundred picoseconds. In low concentration solution, after the interchain transfer is complete, intrachain migration is too slow for the exciton to move enough distance during its lifetime to change the orientation of the transition dipole. This leads to plateaus in the time-resolved anisotropies for both low concentration solutions, as observed in Fig. 4. However, after rapid interchain transfer in high concentration solution, exciton migration along the backbone for small distances increases the likelihood of finding a lower energy chromophore on a nearby chain within the Förster radius. This allows additional interchain transfer to occur on a time scale of a few hundred picoseconds, rate-limited by intrachain energy migration.

The much slower energy migration along a conjugated polymer chain by roughly two orders of magnitude as compared with energy transfer between conjugated polymer chains has important implications for devices based on these materials. Recent work by Warman and co-workers has found that the intrachain mobility of single carriers (electrons or holes) on isolated MEH-PPV chains is enormous—more than four orders of magnitude larger than the carrier mobility observed by time-of-flight measurements in conjugated polymer devices (41). This result suggests that transport of electrically charged carriers is facile along a conjugated polymer chain but slow between chains, the opposite of what we have found here for energy transfer (exciton migration). In combination, these results suggest that with proper control over chain conformation and interchain interactions (30), we can greatly increase the

efficiency of devices based on conjugated polymers. In our current generation of polymer-based devices, the slow hopping of carriers between chains limits the current that can be transported through an amorphous polymer film. Moreover, once the carriers do recombine to form excitons, rapid interchain energy transfer likely causes the newly formed exciton to migrate to a low energy defect or trap site, quenching the luminescence.

In contrast, a device based on electrical contact to isolated polymer chains such as those encapsulated in the mesoporous glass would have efficient charge transport along the chain, and thus the current would not be limited by hopping of carriers between chains. After injected electrons and holes recombine on a single chain, the newly formed exciton would not be able to migrate a significant distance along the backbone during its lifetime, reducing the probability of quenching at defect sites. Even without direct electrical contact to single chains, a device utilizing energy transfer into the isolated polymer segments within the pores would have a significantly enhanced efficiency. The strong dependence of the optical properties of conjugated polymers on chain conformation opens a range of opportunities to use nanoscale architecture to control polymer structure and thus direct energy migration in these materials.

#### References and Notes

- See, e.g., M. Orritt, *Science* **285**, 349 (1999), and references therein.
- M. A. Fox, *Acc. Chem. Res.* **32**, 201 (1999), and references therein.
- D. M. Kaschak et al., *J. Am. Chem. Soc.* **121**, 3435 (1999).
- D. M. Kaschak and T. E. Mallouk, *J. Am. Chem. Soc.* **118**, 4222 (1996).
- See, e.g., R. H. Friend et al., *Nature* **397**, 121 (1999).
- L. J. Rothberg and A. J. Lovinger, *J. Mater. Res.* **11**, 3174 (1996).
- C. T. Kresge et al., *Nature* **359**, 710 (1992).
- J. S. Beck et al., *J. Am. Chem. Soc.* **114**, 10834 (1992).
- R. Kersting et al., *Phys. Rev. Lett.* **70**, 3820 (1993).
- U. Lemmer et al., *Chem. Phys. Lett.* **209**, 243 (1993).
- G. R. Hayes, I. D. W. Samuel, R. T. Phillips, *Phys. Rev. B* **52**, R11569 (1995).
- R. Kersting et al., *J. Lumin.* **72-74**, 936 (1997).
- Ch. Warmuth et al., *J. Lumin.* **76-77**, 498 (1998).
- See, e.g., P. Bolivar et al., *Chem. Phys. Lett.* **245**, 534 (1995), and (17–19).
- A. Dogariu, R. Gupta, A. J. Heeger, H. Wang, *Synth. Met.* **100**, 95 (1999).
- G. Cerullo et al., *Synth. Met.* **101**, 306 (1999).
- M. Wohlgenannt et al., *Chem. Phys.* **227**, 99 (1998).
- See R. Kersting et al., *J. Chem. Phys.* **106**, 2850 (1997), and references therein.
- T. Förster, *Ann. Phys.* **2**, 55 (1948).
- T.-Q. Nguyen, V. Doan, B. J. Schwartz, *J. Chem. Phys.* **110**, 4068 (1999).
- C.-G. Wu and T. Bein, *Science* **266**, 1013 (1994).
- , *Science* **264**, 1757 (1994).
- K. Moller, T. Bein, R. X. Fischer, *Chem. Mater.* **11**, 665 (1999).
- K. Kageyama, J. Tamazawa, T. Aida, *Science* **285**, 2113 (1999).
- J. J. Wu, A. F. Gross, S. H. Tolbert, *J. Phys. Chem. B* **103**, 2374 (1999).
- A. Firouzi et al., *J. Am. Chem. Soc.* **119**, 9466 (1997).
- S. H. Tolbert, A. Firouzi, G. D. Stucky, B. F. Chmelka, *Science* **278**, 264 (1997).
- Many groups have observed differing excited state absorption dynamics in solutions versus films of PPV-

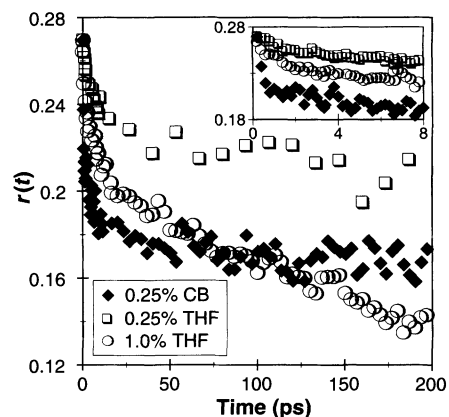


**Fig. 4.** Ultrafast stimulated emission anisotropy (Eq. 1) of MEH-PPV in three different solution environments: low concentration in CB ( $\blacklozenge$ ), low concentration in THF ( $\square$ ), and high concentration in THF ( $\circ$ ). Concentrations are given in weight per volume. Pump and probe wavelengths are the same as in Fig. 3. The inset shows the early time dynamics on an expanded scale.

- based polymers; see, e.g. (29) or (30). However, the origin of this difference is controversial and may depend on photooxidation of the sample or the intensity of the excitation beam in addition to inter-chain effects; see, e.g. (30–32). No matter how the effect arises, under the conditions of our experiments, the decay of MEH-PPV's excited state absorption is different in solution and film environments (Fig. 2). Thus, we can use excited state absorption to help determine the local environment of the polymer in different regions of the composite sample.
29. M. Yan, L. J. Rothberg, E. W. Kwock, T. M. Miller, *Phys. Rev. Lett.* **75**, 1992 (1995).
  30. T.-Q. Nguyen, I. Martini, J. Liu, B. J. Schwartz, *J. Phys. Chem. B* **104**, 237 (2000).
  31. N. T. Harrison, G. R. Hayes, R. T. Phillips, R. H. Friend, *Phys. Rev. Lett.* **77**, 1881 (1996).
  32. V. I. Klimov, D. W. McBranch, N. N. Barashkov, J. P. Ferraris, *Chem. Phys. Lett.* **277**, 109 (1997).
  33. The polarization notation used throughout this report is

- as follows: the first character indicates the pore direction in the lab frame (always vertical in this report), the second character indicates the lab polarization of the excitation beam, and the third character denotes the collection or probe polarization direction. For example, VHV indicates excitation light polarized perpendicular to the pore direction but collection or probe light polarized along the pore channels.
34. C. R. Cantor and P. R. Schimmel, *Biophysical Chemistry, Part II* (Freeman, San Francisco, CA, 1980), p. 474.
  35. The single exponential fit is not representative of a particular model for intrachain energy transport; rather, it is merely a way to define a characteristic time for the anisotropy increase. Because the anisotropy at long times is computed from the ratio of two small numbers (Eq. 1 at times after most of the excitons have decayed), we do not feel that the signal-to-noise ratio of the anisotropy increase justifies fitting to a more complex model with a higher number of parameters.

36. C. Weder, C. Sarwa, C. Bastiaansen, P. Smith, *Adv. Mater.* **9**, 1035 (1997).
37. G. R. Hayes, I. D. W. Samuel, R. T. Phillips, *Phys. Rev. B* **56**, 3838 (1997).
38. A. Watanabe, T. Kodaira, O. Ito, *Chem. Phys. Lett.* **273**, 227 (1997).
39. A. Ruseckas *et al.*, *J. Lumin.* **76-77**, 474 (1998).
40. J. Z. Zhang *et al.*, *J. Chem. Phys.* **106**, 3710 (1997).
41. R. J. O. M. Hoofman, M. P. deHaas, L. D. A. Siebbeles, J. M. Warman, *Nature* **392**, 54 (1998).
42. Supported by the Petroleum Research Fund, administered by the ACS (grants 32773-G6 and 33715-G5); the Office of Naval Research (grant N00014-99-1-0568); the NSF (grant DMR-9971842). B.J.S. is a Cottrell Scholar of Research Corporation and an Alfred P. Sloan Foundation Research Fellow. We thank F. Wudl and R. Helgeson for providing the MEH-PPV used in this work.

2 September 1999; accepted 2 March 2000

# A Superconducting Field-Effect Switch

J. H. Schön,<sup>1</sup> Ch. Kloc,<sup>1</sup> R. C. Haddon,<sup>2</sup> B. Batlogg<sup>1</sup>

We report here on a novel realization of a field-effect device that allows switching between insulating and superconducting states, which is the widest possible variation of electrical properties of a material. We chose  $C_{60}$  as the active material because of its low surface state density and observed superconductivity in alkali metal-doped  $C_{60}$ . We induced three electrons per  $C_{60}$  molecule in the topmost molecular layer of a crystal with the field-effect device, creating a superconducting switch operating up to 11 kelvin. An insulator was thereby transformed into a superconductor. This technique offers new opportunities for the study of superconductivity as a function of carrier concentration.

The basic idea of an ideal electric “valve” goes back to the late 1920s and involves switching between high- and low-resistance regimes by an applied electric field (1). However, reliable devices could not be prepared until 30 years later (2), surface states of inorganic semiconductors, such as silicon or germanium, being the major hurdle. Since then, the silicon field-effect transistor (FET) has become the cornerstone of modern semiconductor industry and technology. In addition, there has been an ongoing effort to modulate superconductivity in thin films by an applied static electric field (3). Shifts of the transition temperature  $T_c$  of up to 30 K have been observed in high- $T_c$  cuprate films, caused by changing the concentration of charge carriers in the electronically active  $CuO_2$  layers (4, 5). However, complete field-induced switching between superconducting and insulating states remains a desirable goal. Here we report on a novel  $C_{60}$ -based field-effect device, an ultimate switch between the insulating and superconducting regimes of chemically pure  $C_{60}$ .

Working with  $C_{60}$  as the starting material is advantageous because so much is known about transport, and ultimately superconductivity, in  $C_{60}$  when electrons are induced by chemical doping (6, 7). Undoped  $C_{60}$  has a band gap of approximately 2 eV and is therefore insulating, whereas alkali metal-doped  $C_{60}$  ( $A_3C_{60}$ ) exhibits metallic conductivity and, at low temperatures, superconductivity. Furthermore, working with van der Waals-bonded materials, such as molecular crystals, offers the inherent advantage of low surface state densities because of the absence of dangling bond-type surface states. Previous studies on organic semiconductors such as pentacene have shown that in an organic FET the chemical potential can be shifted easily across the band gap of the semiconductor, leading to  $n$ - as well as  $p$ -channel activity (8).

We have grown  $C_{60}$  single crystals that are several  $mm^3$  in size in a stream of hydrogen in an apparatus similar to that used for the growth of other organic semiconductor crystals (9). Multiply sublimed material was used as a starting material. In order to prepare field-effect devices on  $C_{60}$  single crystals, we evaporated gold source and drain contacts on smooth growth surfaces through a shadow mask. Channels were typically 25 to 50  $\mu m$  long and 500 to 1000  $\mu m$  wide. Sputtered  $Al_2O_3$  with a capac-

itance  $C_i$  of 185 nF/cm<sup>2</sup> was used as the gate dielectric. Finally, a gold gate electrode was deposited on top of the oxide (Fig. 1). FET measurements were carried out in vacuum at temperatures between 4 and 300 K. Additional space charge-limited current measurements were used to determine the number of electrically active defects in these high-quality single crystals (10). Trap concentrations (deep levels) as low as  $3 \times 10^{12} \text{ cm}^{-3}$  (one per  $5 \times 10^8 C_{60}$  molecules) are estimated. This level is significantly lower than those reported earlier for other vacuum-grown crystals (11).

Previous thin film  $C_{60}$  transistors exhibited  $n$ -type behavior and field-effect mobilities of 0.09  $\text{cm}^2/\text{V}\cdot\text{s}$  (12). Figure 1 shows the typical transistor characteristics at room temperature for single-crystal devices. These devices show  $n$ - as well as  $p$ -channel activity, reflecting the ambipolar transport in these high-quality single crystals and further emphasizing the low interface state density of the FET. Electron and hole mobilities of 2.1 and 1.8  $\text{cm}^2/\text{V}\cdot\text{s}$ , respectively, are deduced from standard semiconductor equations (13). At room temperature, the channel resistance can be varied over approximately nine orders of magnitude by the applied gate bias (Fig. 2A). Figure 2A shows the channel resistance as a function of gate charge ( $n = C_i V_g / e$ , where  $n$  is the charge carrier density,  $C_i$  is the capacitance,  $V_g$  is the gate voltage, and  $e$  is the elementary charge) at room temperature and 5 K. The initial drop of the resistance at a few volts reflects the turn-on of the FET. At larger bias, charge accumulates in the channel, leading to a gradual decrease of the resistance. Finally, at very high positive gate voltages, the channel resistance drops abruptly to zero below a critical temperature  $T_c$  of 11 K. The channel evidently becomes superconducting. The drop of the resistance depends both on the applied gate voltage and on the temperature. This is shown in Fig. 2B, where the channel resistance is plotted versus temperature and the gate charge. A priori we do not know the electronic nature of the superconducting channel; that is, how many molecular layers become supercon-

<sup>1</sup>Bell Laboratories, Lucent Technologies, 600 Mountain Avenue, Murray Hill, NJ 07974, USA. <sup>2</sup>Departments of Chemistry and Physics and Advanced Carbon Materials Center, University of Kentucky, Lexington, KY 40506, USA.